Polymer Testing 116 (2022) 107770

Contents lists available at ScienceDirect

Polymer Testing

journal homepage: www.elsevier.com/locate/polytest

Manufacturing and toughening effects on the material properties of wind turbine blade adhesives

Dharun Vadugappatty Srinivasan, Anastasios P. Vassilopoulos *

Composite Construction Laboratory (CCLab), Ecole Polytechnique Fédérale de Lausanne (EPFL), Station 16, CH-1015, Lausanne, Switzerland

ARTICLE INFO

Keywords:
Wind turbine blade
Composites
Epoxy adhesive
Toughening
Void
Failure analysis

ABSTRACT

Hybrid adhesives can be developed using commercially available adhesive materials and customized to the required loading conditions. In this paper, SPABOND™ 820HTA (non-toughened) and SPABOND™ 840HTA (toughened) adhesives are hybridized by two strategies and fabricated by machine and manual mixing methods. The manufacturing and hybridization effects on the bulk adhesive properties are evaluated by dynamic mechanical analysis, quasi-static tensile, V-notch shear and single-edge-notch bending tests. X-ray micro-computed tomography, digital image correlation technique, high speed camera and scanning electron microscopic images are used for assessing the manufacturing quality, computing the full-field displacement and strain, and failure analysis. By considering the manufacturing methods, the measured properties are less influenced by the presence of voids but dependent on the glass fiber filler orientation. The adhesive toughening method improves the strain to failure and tensile toughness, decreases the strength and modulus and no significant effect on the glass transition temperature.

1. Introduction

Renewable energy is probably the most prominent solution to global climate change and to attain the carbon neutral goal by 2050. Wind and solar energy are expected to share at least two thirds of renewables growth. The wind energy saw 17% increase in 2021, translating additional 275 TWh energy generation as compared to 2020 [1]. Thanks to rapid industrialization and increasing wind turbine blade size, the installation were ramped up and the installed energy has seen a rise of 84 GW in between 2001 and 2020 [2]. The composite wind turbine blade shells, spar caps, shear webs and sandwich foams are assembled with structural adhesives. As the blade size increases significantly, the adhesive joint design and bonding process become challenging. The blades are subjected to static, impact, fatigue, and environmental loadings during their service life [3–8]. Non-toughened and toughened epoxy adhesives are commonly used due to their inherent mechanical and chemical properties [9]. Typically, non-toughened epoxy adhesives have higher mechanical stiffness, strength and cost-effectiveness as compared with the toughened adhesives, while non-toughened adhesives possess poor strain to failure, poor crack and impact resistance that can be improved by adhesive toughening. Epoxy adhesives are commonly modified with toughening particles such as elastomers [10,11] thermoplastic fillers [12,13] natural fillers [14], nanoparticles [15] and co-polymers [16]. Several toughening mechanisms such as rubber particle deformation, multiple crazing, shear yielding and cavitation, crack pinning was discussed in Ref. [17]. Nevertheless, toughening introduces flexible materials and chains inside the rigid epoxies, and it may reduce other mechanical properties such as tensile modulus and tensile strength as well as the temperature-related performance [18]. Alternatively, rigid phases such as nano-silica core-shell particles can be used to overcome this issue [19]. Moreover, toughened adhesives are not cost-effective in high-volume applications. For instance, in wind turbine blades, the adhesive bond line thickness can be up to 30 mm whereas the bond length is in the range of a few 10 m [9,20]. Implementing these high-cost toughening strategies in the large bond volume applications is not practically feasible. For this reason, hybrid adhesives with desirable mechanical properties should be developed using commercially available adhesives. Therefore, further certification of these adhesives is not required and can be readily used by the blade manufacturers. For example, a typical wind turbine adhesive product needs shop approval, adhesive system type approval and component certification, as mentioned in Refs. [21–23].

Hybrid adhesives are preferred in tailoring the adhesive joints [24]. To exemplify, a non-toughened adhesive having higher tensile modulus

* Corresponding author.
E-mail address: anastasios.vassilopoulos@epfl.ch (A.P. Vassilopoulos).

https://doi.org/10.1016/j.polymertesting.2022.107770
Received 20 July 2022; Accepted 1 September 2022
Available online 6 September 2022

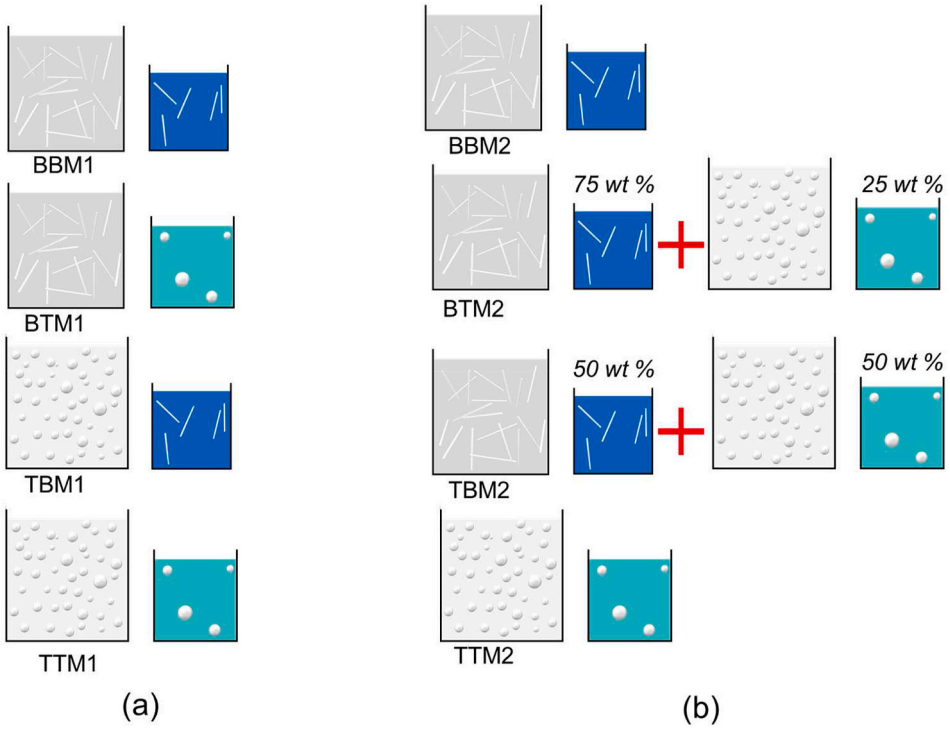

Fig. 1. Schematic diagram of the adhesive material composition: (a) M1, machine mixing method and (b) M2, manual mixing method.

was locally tailored with a lower tensile modulus adhesive, in the load critical areas [25]. Thus, the shear strength of the composite adhesive joints can be increased due to a reduction in the edge peel stresses [26]. Stress concentrations also occur at bi-material joints due to a mismatch in material modulus that may result in unstable crack propagation [27]. To tailor the desired crack path, these hybrid adhesives can be carefully placed in the bonded joints. Previous studies confirmed that adhesive intermingling and chemical compatibility during the curing process as major concerns in developing multi-adhesive tailored joints [28]. Consequently, a combination of new adhesives needs to be investigated to overcome the above challenges.

The apparent shear strength measured by the in-situ shear testing was independent of the joint thickness unlike the butt-tensile strength. The increase in butt-tensile strength due to increase in joint thickness can be explained by the varying adhesive stresses along the bond line [29]. The study of bulk adhesive properties is critical to derive the failure criterion [30] and model the behavior of thick adhesive joints and only limited data available in the literature [31].

Two-component epoxy adhesives (base and hardener) in paste forms are highly viscous and mixed by a mechanical mixer before applying to the bonding surface. This technique is practiced by blade manufacturers to avoid voids and control the bond quality, although it is not eliminating voids. In other scenarios such as adhesively bonded local repair process and academic research, manual mixing is followed. In this technique, the adhesive and hardener are poorly mixed, and voids are introduced while mixing or adhesive deposition process. Because of voids, the bulk adhesive tensile strength and failure strain were decreased by 24.87%. Although, the presence of voids was visualized by high-resolution X-ray microscope, their size and volume distribution were not compared quantitively [32]. In case of notched tensile testing, the tensile strength of hand mixing specimens was 30% lesser than the dispenser mixed specimens [33]. Defects in glass filler modified epoxy adhesives affect the stress distribution inside the material which act as potential crack initiation sources [34]. Apart from manufacturing quality, the adhesive processing conditions such as degassing, curing, and post-curing affect the performance [35,36]. For example, lowering the curing time and cool-down time resulted a decrease in tensile modulus, tensile strength, and fracture energy [37]. The post-curing of adhesives could increase the tensile strength by at least 11% as compared to the non-post-cured specimens. The scatter in strength (13%) was also higher in the experimented tests. Bulk adhesive forms were also used to assess the environmental aging and moisture effects on the fatigue life [38,39]. Given the above literature studies, it is justified that the bulk adhesives could be exploited to estimate the effect of different studying parameters on the static and fatigue performance.

Most of these studies were focused on the toughening effect on the dynamic mechanical analysis (DMA), tensile and fracture properties but not on the shear strength. The discussed toughening methods could not be readily used by the wind turbine blade manufacturers. For this purpose, new hybridization strategies reducing the certification process, time and cost need to be developed. In this paper, non-toughened and toughened wind turbine adhesives were used to fabricate pristine and hybrid adhesives through two different manufacturing techniques and hybridization strategies. The manufacturing and hybridization effects on the material properties were evaluated by dynamic mechanical analysis (DMA), quasi-static tensile, V-notch shear and single-edge-notch bending (SENB) experiments. X-ray micro-computed tomography (μCT) was exploited to determine the void volume distribution in the adhesives. Further, failure analysis was supplemented with high-speed camera and scanning electron microscopic (SEM) images.

2. Materials and manufacturing

Two different epoxy-based paste adhesives SPABOND™ (SP) 820HTA and SPABOND™ 840HTA provided by Gurit (UK) Ltd were used for fabricating pristine (BBM1, TTM1, BBM2 and TTM2) and hybrid adhesives (BTM1, TBM1, BTM2 and TBM2). SP 820HTA is a glass fiber-filled, non-toughened adhesive (BB) [40] whereas SP 840HTA is toughened with core-shell rubber particles (TT) [41]. Both adhesives were also formulated with non-fibrous fillers to avoid sagging. HTA stands for high-temperature application. This adhesive material system offers lower curing time and higher blade production efficiency as compared to the standard adhesives.

Two different manufacturing methods M1 and M2 are considered in

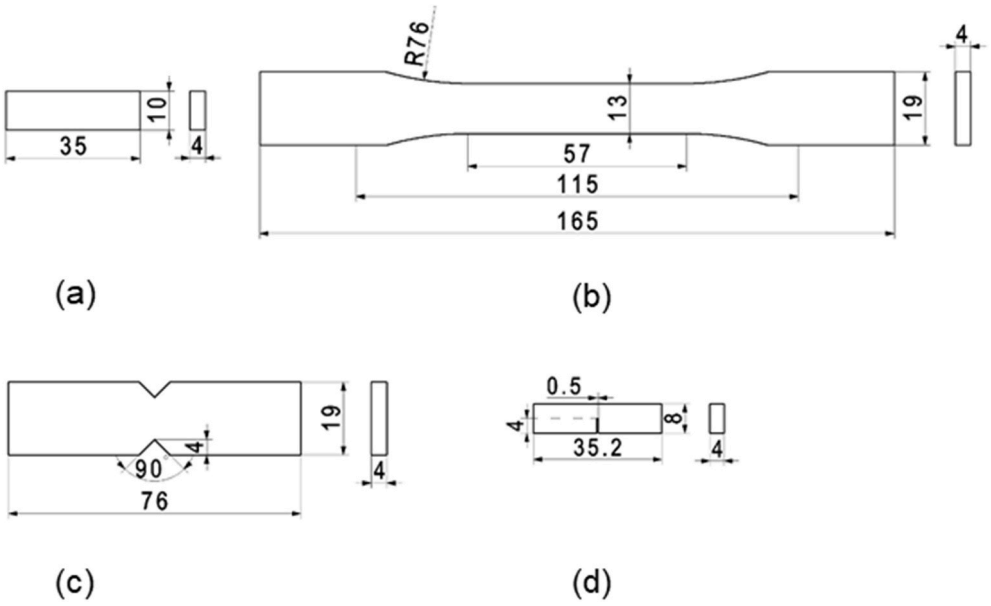

Fig. 2. Geometrical details of the test specimens: (a) DMA, (b) uniaxial tensile, (c) V-notch shear, and (d) SENB.

this study namely, (i) machine mixing (M1) and (ii) manual mixing methods (M2). Method M1 requests the epoxy base and hardener mixed thoroughly using a mechanical mixer at a weight ratio of 100:33, as practiced by the wind turbine industries. The adhesive was poured on the bottom glass plate as a bead and then pressed with the top glass plate for better spreading. A rubber spacer having a diameter of 4 mm was used to control the adhesive plate thickness. M1 panels were fabricated and provided by Gurit (UK) Ltd.

According to method M2, wooden spatulas were used to mix the adhesive materials for 5–7 min by hand and degassed at 0.95 bar of vacuum for around 7 min. After degassing, the adhesive was spread inside an aluminum mold cavity layer by layer, to make an adhesive panel of 4 mm thickness. Preceding this process, the mold plate was coated twice with a mold release agent (Sika® liquid wax- 815) and dried for 15 ± 5 min at the ambient temperature (20 ± 2 °C). The mixed adhesive system was cured at the ambient temperature for 2 h which includes the adhesive mixing and degassing processes, to mimic the time taken by the blade manufacturers for applying adhesive on the long wind turbine blades. Afterwards, the adhesive was heated to 70 °C at a rate of 2 $°C/min$ and cured for 2 h. The same curing cycle was followed for fabricating all the adhesive panels at the facilities of the experimental platform GIS-ENAC of the Ecole Polytechnique Fédérale de Lausanne.

This work also proposes two different hybridization strategies to develop the hybrid adhesives. As illustrated in Fig. 1a, the hardeners of non-toughened (BB) and toughened adhesives (TT) were swapped in the first strategy. In detail, BTM1 hybrid adhesive was prepared by mixing SP 820HTA base and SP 840HTA hardener whereas the combination of SP 840HTA base and SP 820HTA hardener was used in developing TBM1 adhesive. The above strategy is cost-effective, as any one of the hardener and base materials was used for developing new hybrid adhesive. The second hybridization strategy is conventional, i.e., mixing the non-toughened adhesive (base with hardener) and toughened adhesive (base with hardener) at certain weight proportions. Fig. 1b illustrates that the hybrid adhesives, BTM2 and TBM2 were prepared by mixing the toughened adhesive with non-toughened adhesive at 25 wt% and 50 wt %, respectively. Due to confidentiality, the specific details of adhesive chemical composition, glass fiber and the toughening agents name, and volume ratio are not pursued here.

Specimens for DMA, uniaxial tensile, V-notch shear and SENB experiments were cut from the adhesive panels resulted from both manufacturing methods to the required nominal dimensions by an abrasive water jet cutting machine. The dimensions of the test specimens are given in Fig. 2. In SENB specimens, an initial notch of 4 mm was machined by a rotary saw and further sharpened with an abrasive paste and a razor blade. The initial crack length of all the specimens was measured by using an optical microscope, Dino-Lite AD7013MZT, with a 5-megapixel sensor that can magnify 240 times with a resolution of 2592 × 1944 pixels. To implement the digital image correlation (DIC) technique, all the tensile, shear and SENB specimens were uniformly coated at least twice with white paint, dried and then sprinkled with the black speckles.

3. Experimental methods

3.1. Micro-computed tomography (μCT) scanning

Void volume of the adhesives was characterized by μCT-scanning at PIXE platform, EPFL, Switzerland. The Ultratom μCT system from RX solutions is equipped with dual Hamamatsu X-ray sources and could operate in reflection (230 kV) and transmission modes (160 kV). Prior to the scanning, the machine was calibrated against the ghosting and white effects. Adhesive specimens having a nominal dimension of 15 mm × 13 mm x 4 mm were placed on the rotating table, at 10.5 mm from the X-ray source. The distance between the source and the detector was maintained as 620 mm, resulting in a voxel size of 3.5 μm. Here, the reflection target was used with the following parameters: 70 kV and 100 μA. A total of 1632 projections were taken for a complete rotation, for a step size of 0.22° and exposure time of 0.25 s. The μCT images were used to reconstruct the volume including the microstructures and defects using Avizo® software.

3.2. Dynamic mechanical analysis

DMA tests were conducted to determine the manufacturing and hybridization effects on the storage modulus ($E^{'}$), glass transition temperature (T_g) and damping ($tan\,\delta$). Storage modulus ($E^{'}$) and loss modulus ($E^{''}$) are the real and imaginary components of complex modulus (E^{*}), also the ability of a material to store (or return) and lose energy, respectively. The ratio between $E^{'}$ and $E^{''}$ is called as damping ($tan\,\delta$). E^{*} is a response of a sinusoidal force input and measured at every cycle over the desired temperature range.

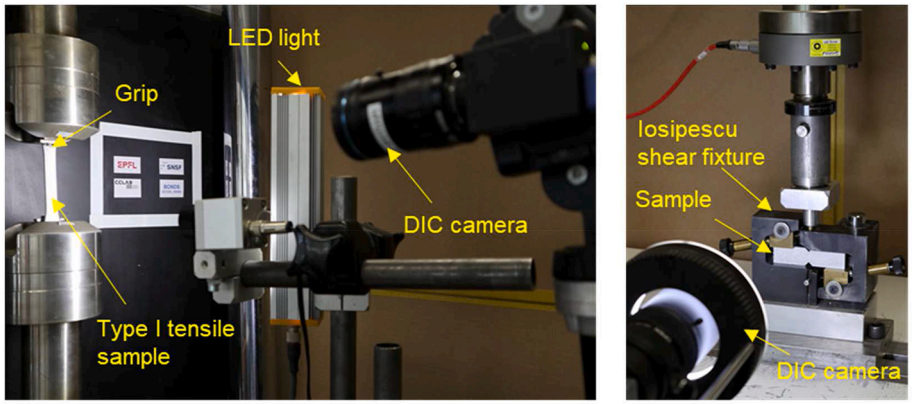

Fig. 3. Experimental test setup: (a) uniaxial tensile and (b) V-notch shear.

DMA specimens were tested under single cantilever mode machine as recommended by ASTM D7028-07 (2015) [42] using TA® Q800 series equipment. Liquid nitrogen was supplied to the test machine for capturing the dynamic mechanical behavior at a lower temperature ($-50\ ^{\circ}C$). The specimen was positioned between the clamps and fastened by applying a torque of 1.47 Nm. At least 3 specimens were tested in each batch in the temperature range of $-50\ ^{\circ}C$ to $150\ ^{\circ}C$ with a heating rate of $5\ ^{\circ}C/min$. The oscillating frequency was set to 1 Hz with an amplitude of 20 μm. The $E^{'}$ and $tan\,\delta$ were measured by the test machine whereas the T_g was calculated from the intersection of two storage modulus slopes in the glass transition region.

3.3. Uniaxial tensile

Uniaxial tensile test was performed using MTS® 810 Landmark servo-hydraulic machine with a calibrated load cell capacity of 5 kN and an applied force accuracy of ±0.2%. The experimental setup is shown in Fig. 3a. ASTM D638-14 Type I specimens [43] were loaded under displacement control at a crosshead displacement rate of 1 mm/min. All the experiments were performed at controlled laboratory ambient temperature ($22 \pm 3\ ^{\circ}C$) and relative humidity of 40 ± 10%. The axial force was measured by the load cell and additionally recorded by an in-house developed LabVIEW® software program. The software interface was also utilized to acquire the testing images for DIC analysis at a frequency of 1Hz. Point Grey – Grasshopper 3 camera (2.2 Megapixels) housing Fujinon HF35SA-1 35 mm F/1.4 lens was employed for capturing the images. The axial strain was computed with VIC 2D-6 software from correlated solutions®. Further, the tensile modulus (E), 0.2% yield strength (σ_y), tensile strength (σ_u), failure strain (ε_f) and tensile toughness (U_T), were calculated from the measured values. The tensile toughness was calculated by integrating the area under the true stress-strain curve. The tensile strength of the adhesives was determined in terms of the peak force (F_{peak}) and the nominal cross-sectional area (A) as follows,

$$\sigma_u = F_{peak}/A_{tensile} \tag{1}$$

3.4. V-notch shear

V-notch shear specimens were prepared as recommended in ASTM D5379-19 [44]. A Walter + bai (w + b) test machine equipped with a load cell capacity of 50 kN and an Iosipescu shear fixture was used to perform the shear experiments as shown in Fig. 3b. The top punch was displacement-controlled at a rate of 1 mm/min. Images were acquired using a Sony XCG-5005E (5 Megapixels) camera with 2448 x 2048 pixels resolution and later analyzed by using the VIC 2D 6 software to obtain the shear strain. The shear modulus was calculated from the slope of the initial linear region of the shear stress-strain diagram. The ultimate shear strength of the adhesives in terms of the peak load (P_{peak}) and cross-sectional area (A_{shear}) can be expressed as,

$$\tau_u = P_{peak}/A_{shear} \tag{2}$$

3.5. Single-edge-notch bending (SENB)

MTS® Acumen equipped with 3 kN load cell and a three-point bending fixture was used for the plane strain fracture toughness experiments. The specimen was adjusted in the fixture such that the initial notch and the contact point of the top roller were in the same loading axis. The crosshead displacement rate of 0.25 mm/min was applied to have a stable fracture. During the testing, the images were captured at a frequency of 0.5 Hz to measure the mid span deflection with DIC. To calculate the effective critical plane strain fracture toughness K_{IC}, the load P_Q was selected as mentioned in ASTM D5045-14 [45]. The fracture toughness, K_{IC} was calculated in terms of the beam thickness (B), width (W), as follows,

$$K_{IC} = \left(\frac{P_Q}{BW^{1/2}}\right) f(x) \tag{3}$$

where. $(0 < x < 1)$

The correction factor f(x) accommodates the influence of initial crack length (a) to the beam width ratio (x) and provided as,

$$f(x) = 6x^{1/2}\frac{[1.99 - x(1-x)(2.15 - 3.93x + 2.7x^2)]}{(1+2x)(1-x)^{3/2}} \tag{4}$$

3.6. High speed imaging and scanning electron microscope

FASTCAM SA- Z, a high-speed imaging camera from Photron® equipped with AF-S NIKKOR 50 mm lens was employed to capture the tensile failure process at 60000 frames per second (fps) and 80000 fps. The same equipment was used to record images at a rate of 70000 fps during the shear experiments. The dynamic crack initiation points and the consequent propagation behavior at different adhesive material systems were analyzed with these images.

The fracture surface of SENB specimens was captured by a ZEISS GeminiSEM 300 microscope at the Interdisciplinary Center for Electron Microscopy (CIME) at EPFL, Switzerland. The fractured specimens were mounted on aluminum stubs holder using a double-side carbon tape and further wrapped with copper tape for better conductivity. The specimens were gold coated and placed inside a vacuum chamber before testing. Totally, 8 different adhesive specimen stubs were fixed to a cylindrical

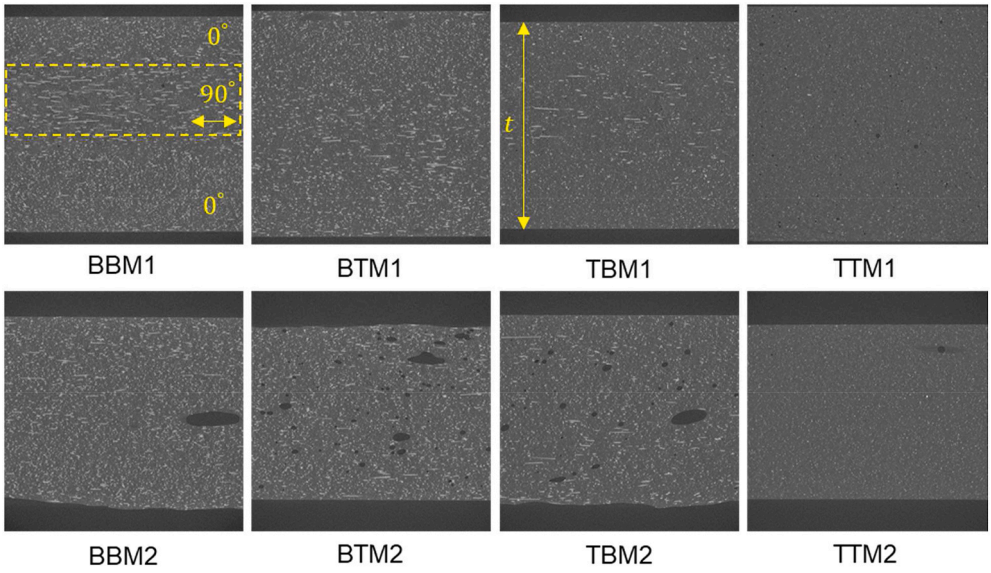

Fig. 4. μCT scanning images of the adhesive materials.

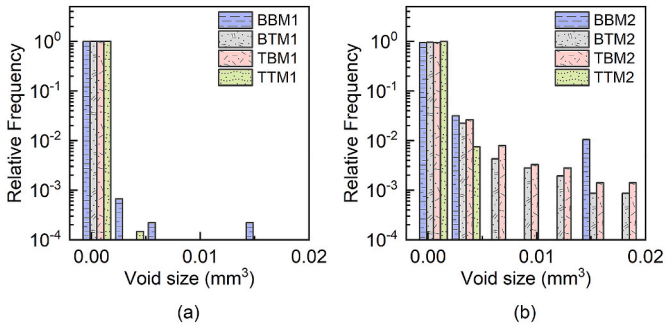

Fig. 5. Logarithmic distribution of the void volume: (a) M1 adhesives and (M2) adhesives.

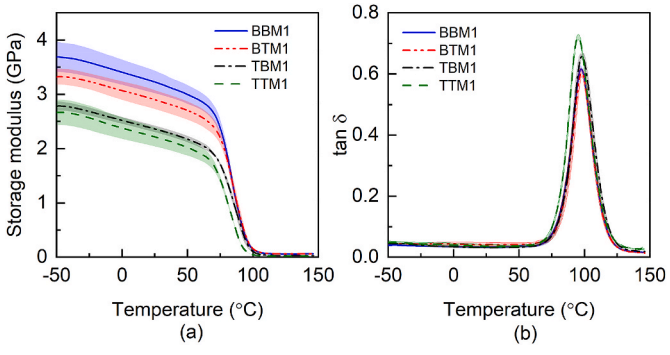

Fig. 6. DMA scan results of epoxy adhesives, M1 method: (a) storage modulus and (b) tan δ.

Table 1
DMA properties of M1 adhesives.

Specimen	T_g (°C)	Peak tan δ (−)	E' at 25 °C (GPa)
BBM1	73.4 ± 0.5	0.623 ± 0.003	3.18 ± 0.17
BTM1	75.4 ± 1.8	0.614 ± 0.014	2.91 ± 0.17
TBM1	74.5 ± 1.6	0.663 ± 0.009	2.36 ± 0.05
TTM1	71.4 ± 0.7	0.723 ± 0.007	2.22 ± 0.15

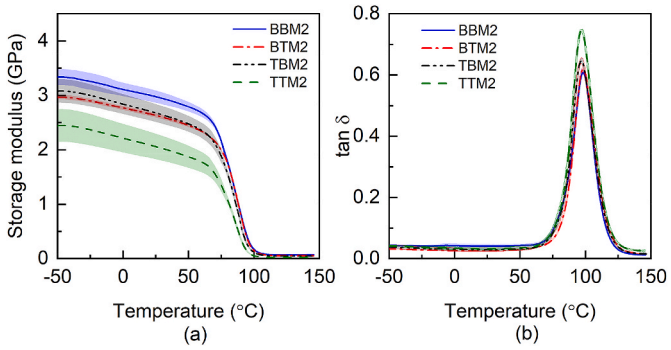

Fig. 7. DMA scan results of epoxy adhesives, M2 method: (a) storage modulus and (b) tan δ.

Table 2
DMA properties of M2 adhesives.

Specimen	T_g (°C)	Peak tan δ	E' at 25 °C (GPa)
BBM2	72.6 ± 0.8	0.613 ± 0.005	2.98 ± 0.10
BTM2	76.9 ± 0.4	0.620 ± 0.007	2.63 ± 0.03
TBM2	76.1 ± 2.9	0.648 ± 0.008	2.68 ± 0.13
TTM2	72.8 ± 1.7	0.748 ± 0.003	2.06 ± 0.20

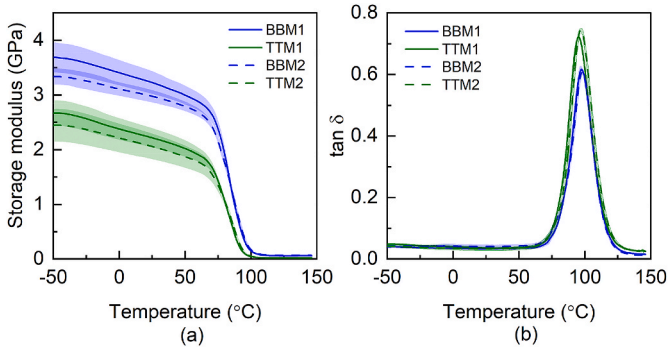

Fig. 8. Comparison of DMA scan results of M1 and M2 methods: (a) storage modulus and (b) tan δ.

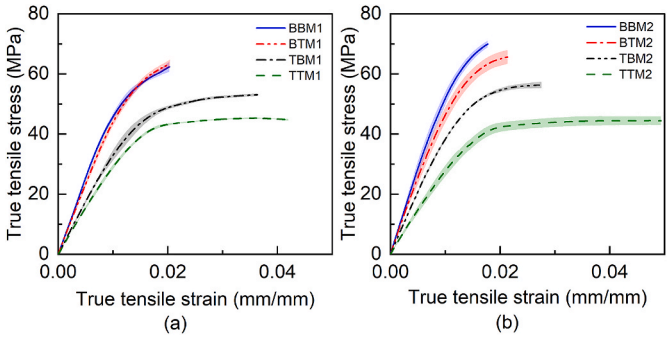

Fig. 9. Uniaxial true tensile stress versus strain response of the adhesives: (a) M1 method and (b) M2 method.

Table 3
Tensile properties of M1 and M2 adhesives.

Specimen	Tensile modulus (E)	0.2% offset Yield stress (σ_y)	Tensile toughness (U_T)	Tensile strength (σ_u)	Failure strain (ε_f)
	GPa	MPa	kJ/m^3	MPa	mm/mm
BBM1	5.1 ± 0.08	51.38 ± 1.89	0.68 ± 0.14	60.16 ± 2.65	0.0179 ± 0.0024
BTM1	4.57 ± 0.22	54.78 ± 1.12	0.69 ± 0.12	61.17 ± 2.18	0.0184 ± 0.0017
TBM1	3.43 ± 0.07	42.20 ± 2.27	1.26 ± 0.17	52.56 ± 0.64	0.0329 ± 0.0027
TTM1	2.98 ± 0.14	38.69 ± 0.89	1.38 ± 0.11	45.36 ± 0.15	0.0391 ± 0.0023
BBM2	5.59 ± 0.39	61.47 ± 1.75	0.71 ± 0.03	69.01 ± 0.51	0.0170 ± 0.0007
BTM2	4.95 ± 0.32	55.65 ± 1.95	0.84 ± 0.10	65.01 ± 2.23	0.0201 ± 0.0010
TBM2	4.02 ± 0.06	47.21 ± 0.39	0.96 ± 0.11	55.98 ± 0.87	0.0248 ± 0.0020
TTM2	2.81 ± 0.16	37.86 ± 0.55	1.45 ± 0.20	44.47 ± 1.26	0.0417 ± 0.0054

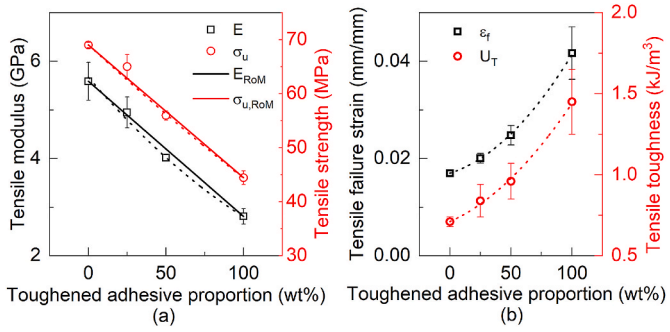

Fig. 10. Hybrid effect of M2 adhesive on the uniaxial tensile properties: (a) modulus and strength and (b) failure strain and toughness.

mount and tested under full vacuum. The electron gun was operated under 5 kV where the stand-off distance was varying from 6.1 mm to 10.4 mm. An aperture size of 30 μm was maintained during the test. Low magnification factors (× 100 and × 500) help to observe the glass fiber orientation, fracture surface texture and the presence of voids. On the other hand, high magnification of these images (× 1300 × 1880 and × 3370) would reveal the fracture mechanisms of the micro-fillers and the sub-micron toughening phase. All imaging parameters are indicated at the bottom of the corresponding images.

4. Results and discussion

4.1. Void characterization

The μCT images depicted in Fig. 4 were randomly selected and show the cross-sectional views of the adhesive materials. 't' refers to the thickness of the different adhesive panels which varies between 3.75 mm and 5.02 mm. The micro constituents such as glass fibers and non-fibrous fillers and defects including micro and macro voids could be seen in these images. In BBM1 specimens, the glass fibers were mostly aligned towards 0° at the outer edges as compared to the highlighted middle section. The glass fibers were also be seen in the hybrid adhesives BTM1, TBM1, BTM2 and TBM2. The little white dots seen in the adhesives including TTM1 and TTM2 adhesives are non-fibrous fillers. Comparing the manufacturing techniques, M2 specimens had more voids and undulated surface than M1 specimens.

Fig. 5a and b shows the relative distribution frequency of the voids in M1 and M2 adhesives in logarithmic scale, respectively.

As visualized in the μCT scanning images, the void size in M1 adhesives is smaller than M2 adhesives. Void size less than 0.005 mm^3 were presented in BTM1, TBM1 and TTM1, whereas voids greater than 0.005 mm^3 were noticed in BBM2, BTM2 and TBM2 adhesives except TTM2. The void volume percentage of M1 adhesives was 0.01%–0.26%. In case of M2 adhesives, the void volume percentage varies in between 0.01% and 3.74%. Therefore, machine dispensed M1 method provides better quality of specimens, as compared to M2 method.

4.2. Hybridization and manufacturing effects on DMA properties

The storage modulus (E') and tanδ versus temperature sweep response of the M1 adhesives are depicted in Fig. 6a and b, respectively. The averaged curves and the associated standard deviation were plotted using OriginPro® 2022 software. The adhesives exhibited three distinct regions, namely glassy (<60 °C), transition (60 °C–100 °C) and rubbery region (>100 °C). In the glassy region, there was a gradual reduction in E' and no momentous change in tan δ. As the temperature increases, the polymeric molecules slowly secure more free volume resulting to molecular motion. Following that, E' was decreased steeply due to the main chain motion whereas the tan δ was increased to a maximum value in this transition region. In the rubbery region, a plateau at low value was observed for both E' and tan δ curves indicating a large scale motion of the chains.

Glass transition temperature, peak tan δ and E' at 25 °C of the M1 adhesives are given in Table 1. Within the experimental scatter, T_g of all the adhesives lies between 71.4 °C to 75.4 °C and there was no significant effect of the first hybridization strategy on T_g. The non-toughened adhesive (BBM1) has higher E' and lower tan δ than the hybrid (BTM1 and TBM1) and toughened (TTM1) adhesives. Due to higher toughening content, the storage modulus of TBM1 adhesive was 23% lesser than BTM1 adhesive. tan δ curve of TBM1 and TTM1 was crossed over the other two adhesives (BBM1 and BTM1) at the transition region, because of their low molecular weight.

Fig. 7a and b illustrate the E' and tan δ response of M2 adhesives. As the proportion of the toughened adhesives was increased from 0% (fully non-toughened, BBM2) to 100% (fully toughened, TTM2), the E' has decreased and vice-versa for the tan δ. T_g was not significantly affected by the second hybridization strategy (refer Table 2) implicating that these non-toughened and toughened adhesives can be mixed or cured together for developing tailored adhesive joints.

Fig. 8 depicts the comparison of the DMA behavior of non-toughened and toughened adhesives fabricated through M1 and M2 methods. E' at 25 °C of BBM1 is 6.3% higher than BBM2 adhesive and there is no significant difference between the measured DMA properties between the machine and manual mixing techniques. However, the high standard deviation (shaded region) of the same adhesive material can be

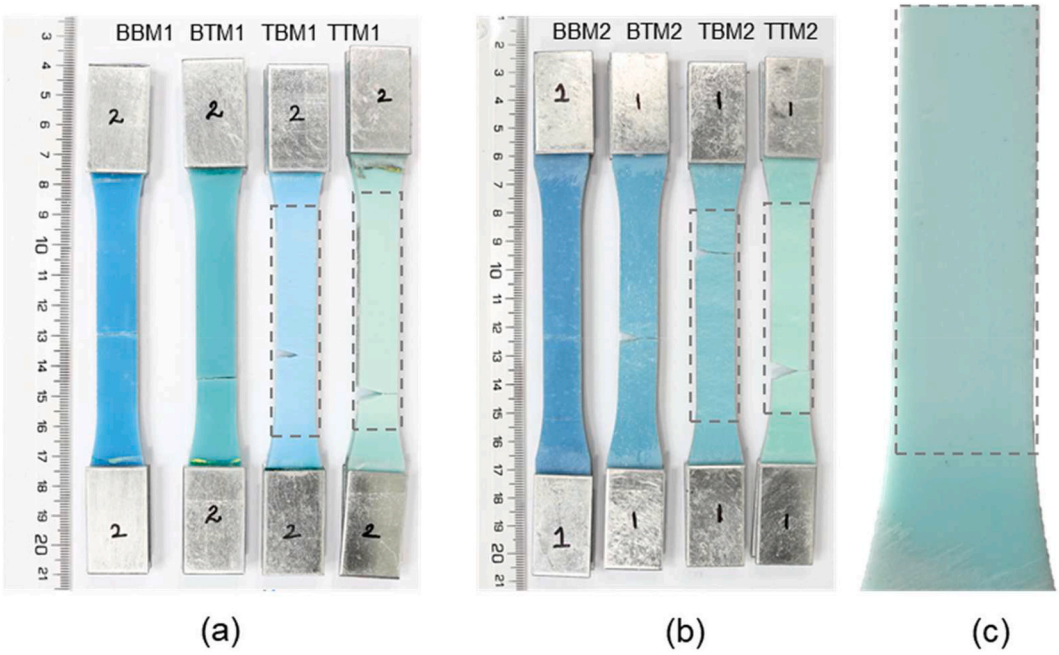

Fig. 11. Failure images of the tensile specimens (a) M1 adhesives and (b) M2 adhesives (c) transition region of TTM2 near the end tab.

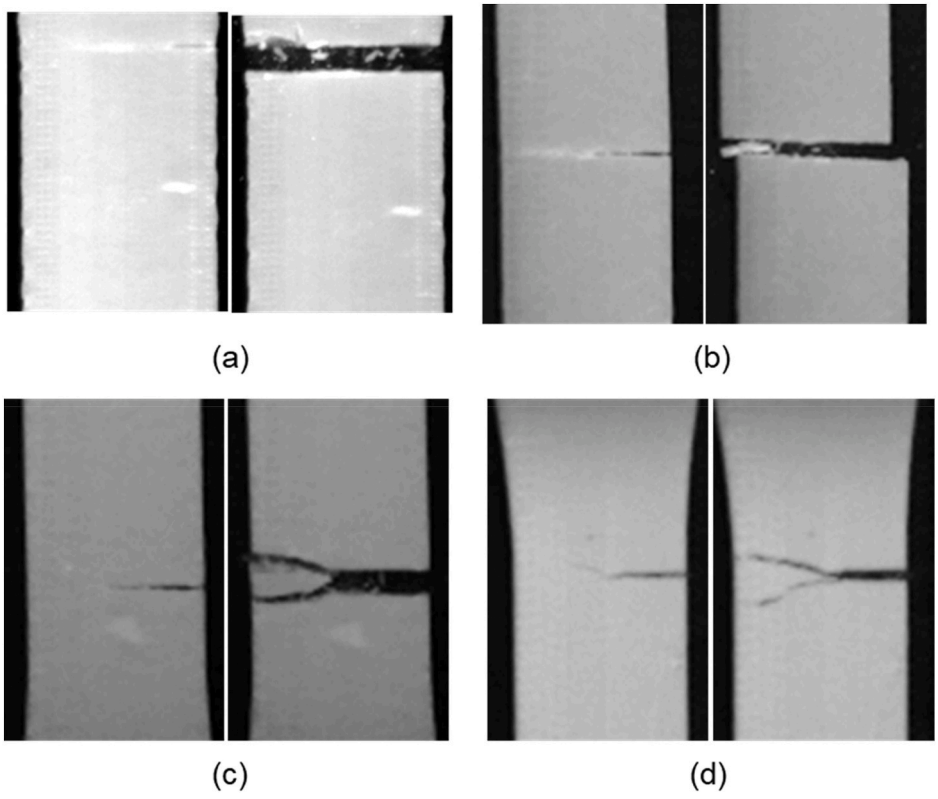

Fig. 12. High speed imaging of the adhesives during final failure initiation: (a) BBM1, (b) BTM1, (c) TBM1 and (d) TTM1 (https://drive.switch.ch/index.php/s/7X8XZeIbuZIPnOg).

attributed to the non-uniform specimen thickness, variation in the clamping force and clamping angle, as discussed by Schalnat et al. [46].

4.3. Hybridization and manufacturing effects on tensile properties

The average true tensile stress versus true tensile strain response of M1 and M2 adhesives are depicted in Fig. 9a and b, accordingly.

As the strain increased, the stress was also increased linearly in the pristine and hybrid adhesives. This linear relationship was described by the tensile modulus using 0.2% yield criteria. Further increase in strain was resulted to a non-linear behavior that can be identified by the yield stress. The tensile properties of the adhesives are provided in Table 3.

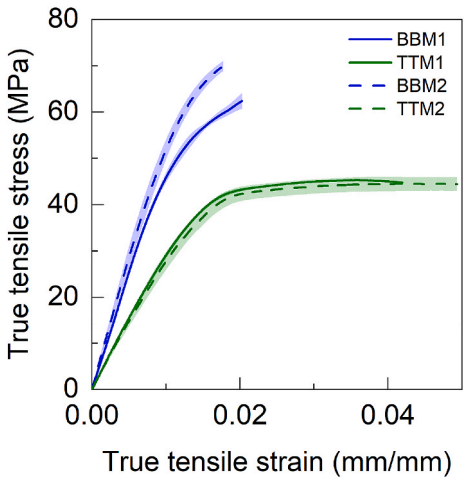

Fig. 13. M1 and M2 manufacturing effect on the tensile behavior of adhesives.

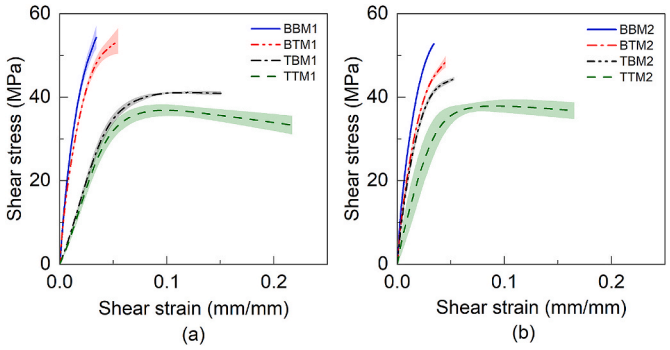

Fig. 14. Shear stress versus shear strain response of the adhesives: (a) M1 method and (b) M2 method.

Table 4
Shear properties of M1 and M2 adhesives.

Specimen	Shear modulus (G)	Shear strength (τ_u)	Failure shear strain (γ_f)
	GPa	MPa	mm/mm
BBM1	2.12 ± 0.19	51.02 ± 1.79	0.0601 ± 0.0102
BTM1	1.13 ± 0.03	51.50 ± 1.14	0.0695 ± 0.0019
TBM1	0.80 ± 0.04	41.19 ± 0.20	0.1316 ± 0.01
TTM1	0.73 ± 0.06	36.91 ± 1.11	0.1574 ± 0.0431
BBM2	1.90 ± 0.50	51.65 ± 1.70	0.0539 ± 0.0035
BTM2	1.63 ± 0.06	46.54 ± 0.34	0.0399 ± 0.0042
TBM2	1.57 ± 0.05	43.03 ± 0.29	0.0435 ± 0.0013
TTM2	0.91 ± 0.09	38.10 ± 1.31	0.12 ± 0.03

The tensile modulus of BBM1 adhesive is 10.4%, 32.7% and 41.6% higher than BTM1, TBM1 and TTM1 adhesives, respectively. The yield stress of BTM1 adhesive was 6.2% lower than the BBM1 adhesive. After yielding, the micro-cracks inside the non-toughened adhesive were continued to grow, resulting a decrease in the tensile modulus. Coalescence of these micro-cracks and glass fiber debonding led to the sudden fracture of the material. While considering the first hybridization strategy, TBM1 adhesive shows a distinct elastic-plastic tensile behavior than BTM1 adhesive, hence it can be used in the practical applications. TBM1 adhesive is commercially branded as SPABOND™ 830HTA by Gurit (UK) Ltd.

The storage modulus and tensile modulus are the two different properties of a material. From Table 1, Tables 2 and 3, it can be noticed that the storage modulus, $E^{'}$, at 25 °C and the tensile modulus values are

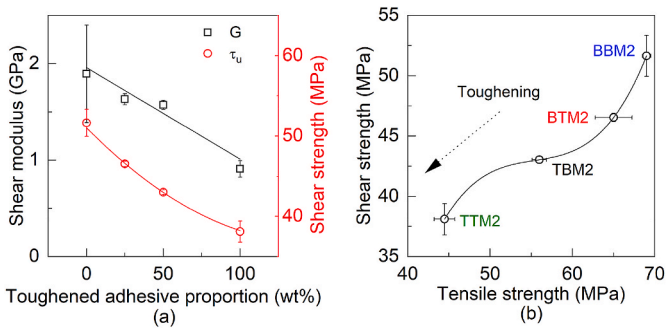

Fig. 15. Shear properties of M2 adhesives (a) effect of toughening and (b) comparison between tensile strength.

not the same. For example, $E^{'}$ of the adhesives vary between 2.06 GPa and 3.18 GPa whereas the tensile modulus of adhesives ranges between 2.81 GPa and 5.59 GPa. As discussed in Section 4.2, $E^{'}$ is calculated from the sinusoidal stress response, periodically whereas E is the initial slope of the linear stress-strain region [47].

Similarly, the average tensile modulus of BBM2 adhesive was 11.4%, 28% and 50% higher than BTM2, TBM2 and TTM2 adhesives, respectively. As the toughened adhesive proportion increases, E and σ_u were decreased non-linearly, refer Fig. 10a. The tensile modulus and strength values predicted by the rules of mixture are plotted as red and black solid lines in Fig. 10a. The predicted values can be validated with the experimentally measured properties. Fig. 10b illustrates the increasing non-linear relationship (dotted curves) of failure strain and tensile toughness with respect to an increase in adhesive toughening proportion. An increase in M2 adhesive toughening was also caused increase in the scattering of the failure strain. It implies that the failure strain of the toughened adhesives is more sensitive to the inherent material defects.

The failure images of the M1 and M2 specimens are shown in Fig. 11a and b, respectively. In case of the hybrid and toughened adhesives, the toughening particles were undergone higher plastic strain and developed more micro-cracks, confirmed by the surface discoloration (whitening). The discoloration was more uniform in TBM1, TTM1, TBM2 and TTM2 adhesives as compared with BTM1 and BTM2. The discolored region was highlighted with the grey dotted boxes in Fig. 11a and b which is attributed to the high volume and distribution of the toughening phase in the adhesive material. The transition between the unaffected elastic region and well plasticized region is shown in Fig. 11c.

The observed small wedge shapes in the failed specimens were resulted from the dynamic crack branching phenomenon. Similar branching was observed in Sikadur-330 adhesives which has a tensile modulus of 4.45 GPa [48]. The high-speed camera images of BBM1 and BTM1 (Fig. 12a and b) depict that an initial dynamic crack was formed at the outer edge of the specimen and propagated perpendicular to the axial loading direction. In TBM1 and TTM1 adhesives (Fig. 12c and d), the primary crack was branched/bifurcated into two secondary cracks. According to Ravichandar et al. [49], the primary crack interacts with the voids or micro-cracks ahead of the crack tip and creates crack instability deviating the crack into branching. The crack branching angle was increased with increase in the adhesive toughening. This phenomenon infers that the toughened adhesive contains more micro-cracks as compared with less or non-toughened adhesives.

Fig. 13 compares the tensile behavior of non-toughened and toughened adhesives manufactured through M1 and M2 methods. There was no effect of manufacturing method on the tensile properties of the toughened adhesive (TTM1 and TTM2). However, the tensile modulus and strength of BBM2 adhesive were by 9.6% and 16.4% higher than those of the BBM1 adhesive respectively, mainly due to the dissimilar orientation of the short glass fiber fillers between them.

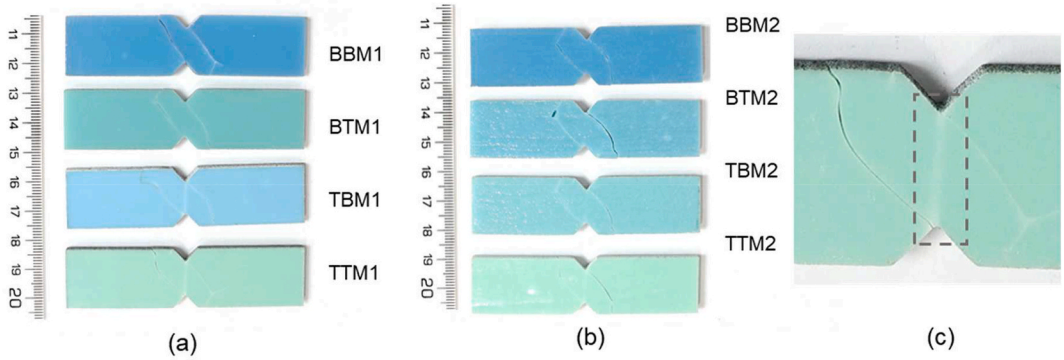

Fig. 16. Failure images of the V-notch shear specimens: (a) M1 adhesives and (b) M2 adhesives.

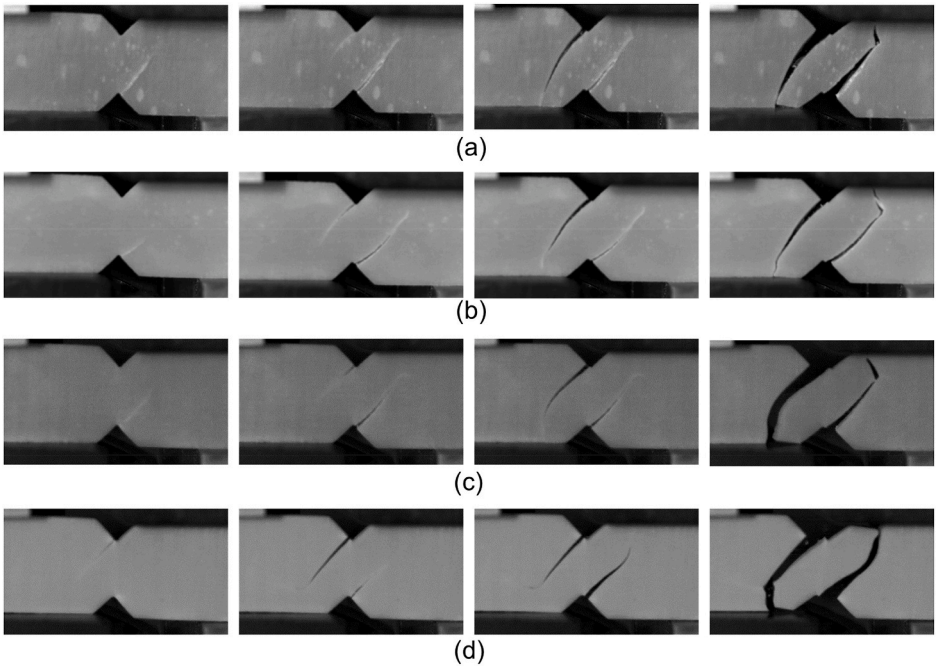

Fig. 17. High speed camera images of the adhesives during shear failure: (a) BBM2, (b) BTM2, (c) TBM2 and (d) TTM2 (https://drive.switch.ch/index.php/s/7X8XZeIbuZIPnOg).

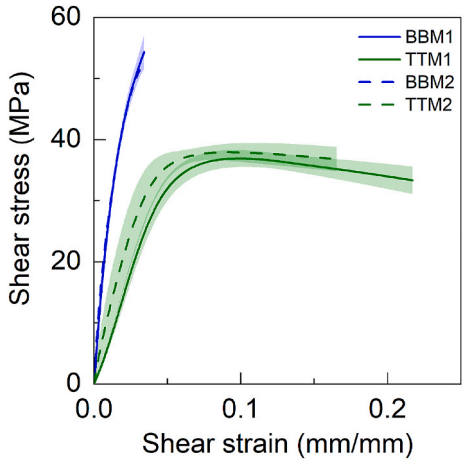

Fig. 18. M1 and M2 manufacturing effect on the shear behavior of adhesives.

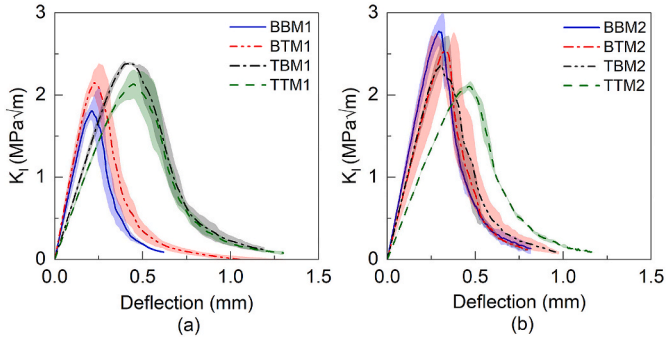

Fig. 19. K_I versus deflection response of the adhesives: (a) M1 adhesives and (b) M2 adhesives.

4.4. *Hybridization and manufacturing effects on shear properties*

The average shear stress versus shear strain response of M1 and M2 adhesives are depicted in Fig. 14a and b, accordingly. As the shear stress

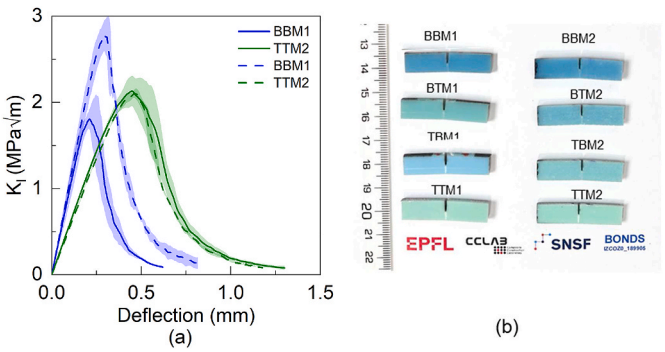

Fig. 20. SENB testing: (a) comparison of M1 and M2 methods and (b) failure images.

was increased, the shear strain increases non-linearly and suddenly failed except TBM1, TTM1 and TTM2 adhesives. These adhesives showed a significant plastic strain of 12%–15.6% before the final failure. In tensile loading, the yield strength depends on the filler type, orientation, and filler-epoxy interface. However, the shear loading is divided into axial and lateral directions and exhibited extensive shear deformation [50]. There is no significant difference between the shear properties of BBM1 and BTM1 adhesives.

The shear modulus, strength and failure strain of the adhesives are given in Table 4. The shear modulus and strength of the adhesives vary between 0.73 GPa and 2.12 GPa and 36.91 MPa–51.65 MPa. The shear strength of BBM1, BTM1 and BBM2 adhesives are around 51 MPa but failed at different shear strain. Based on the required joint stiffness and shear strength, any one of these adhesives can be used in the wind turbine blades.

Fig. 15a depicts that increasing toughening resulted in a linear and

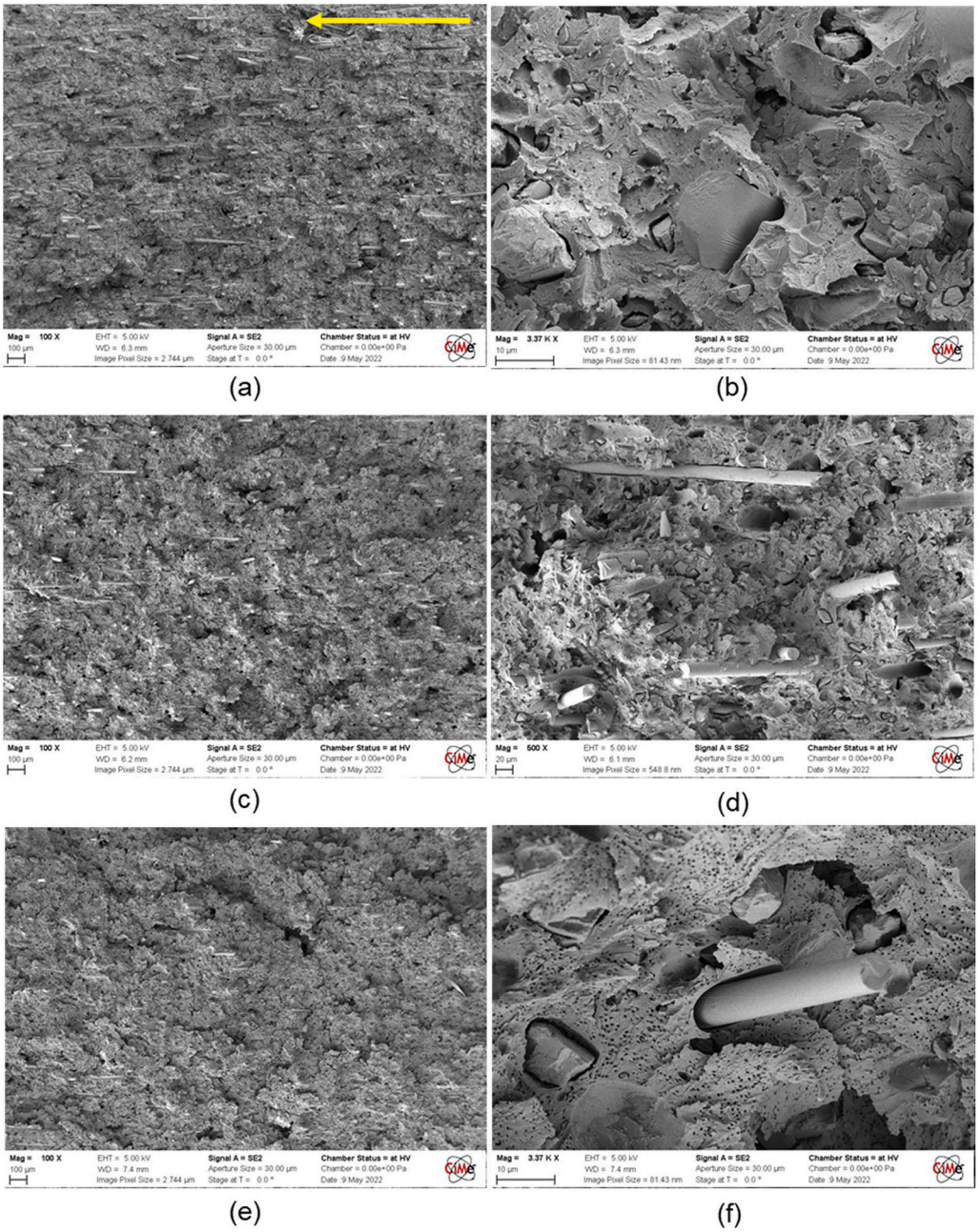

Fig. 21. SEM images of the fractured surface of M1 adhesives: (a)&(b) BBM1, (c)&(d) BTM1 and (e)&(f) TBM1.

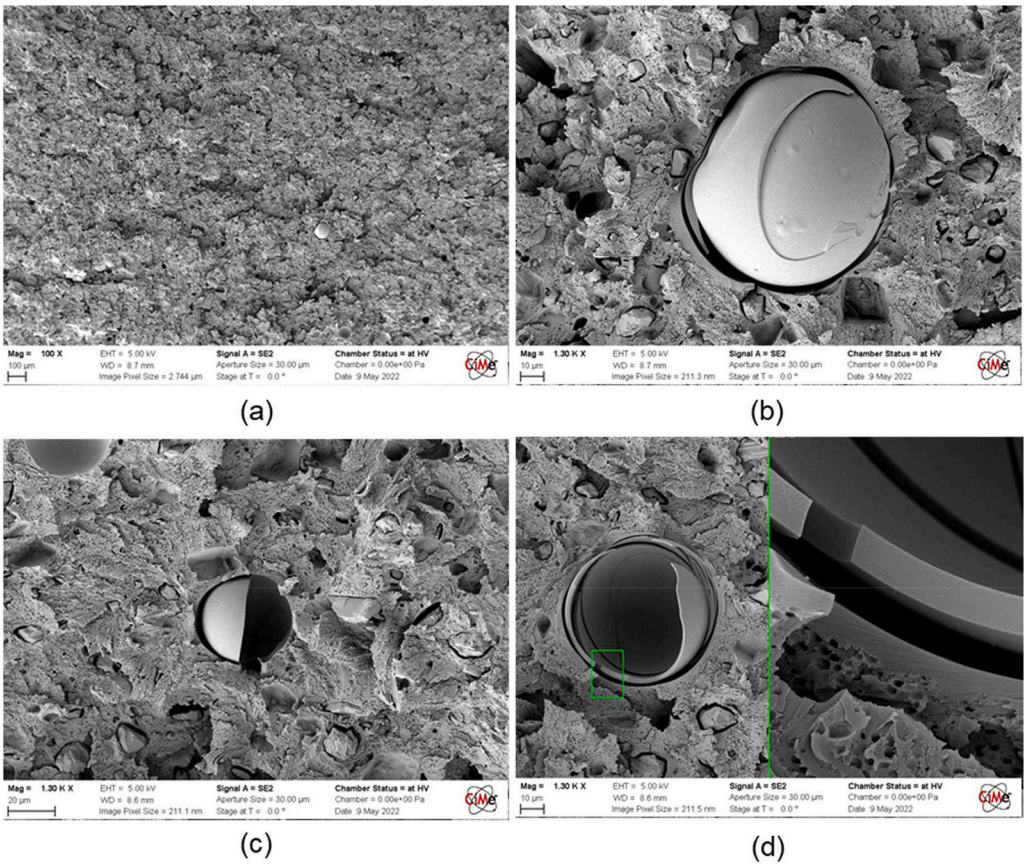

Fig. 22. Fracture surface of TTM1 adhesives: (a) rough fracture surface (b) core of a rubber shell particle (c) complete core failure and (d) multiple tearing at the core wall.

non-linear decrease in shear modulus and shear strength, respectively. The third-order non-linear relationship between the tensile strength and shear strength can be observed in Fig. 15b. As the toughening increases (dotted arrow), the tensile strength decreases at a higher rate as compared to the shear strength.

The shear specimens after the final failure are shown in Fig. 16. As was observed in the tensile specimens, the adhesive whitening due to plasticity was noticed in the toughened adhesives (TBM1, TTM1 and TTM2) as well, showing that the adhesive region in between the notches was under uniform shear stress state.

The dynamic crack initiation and propagation of the BBM2, BTM2, TBM2 and TTM2 adhesives are shown in Fig. 17. Initially, a single crack was initiated from one of the notches and followed by another crack formation from the second notch. The cracks followed relatively a curved path in the less and non-toughened adhesives (BBM2 and BTM2) as compared with the toughened adhesive, TTM2.

The fabrication method did not affect the shear properties of the adhesives, Fig. 18. Within the experimental scatter, the shear modulus and shear strength of these adhesives remained similar.

4.5. Hybridization and manufacturing effects on plane strain fracture toughness

The plane strain fracture toughness (K_I) versus mid-span deflection response of the M1 and M2 adhesives are depicted in Fig. 19a and b, accordingly.

The critical fracture toughness, K_{IC}, of the BBM1, BTM1, TBM1 and TTM1 adhesives are 1.84 ± 0.17 $MPa\sqrt{m}$, 2.12 ± 0.18 $MPa\sqrt{m}$, 2.17 ± 0.05 $MPa\sqrt{m}$ and 1.63 ± 0.05 $MPa\sqrt{m}$, respectively. Within the experimental scatter, the K_{IC} of BBM2 (2.64 ± 0.12 $MPa\sqrt{m}$), BTM2 (2.39 ± 0.17 $MPa\sqrt{m}$) and TBM2 (2.43 ± 0.27 $MPa\sqrt{m}$) adhesives were found to be similar. K_{IC} of TTM2 adhesive is 23.86% lower than the BBM2 adhesive. The fracture toughness of BBM2 and TTM2 adhesives are comparable to the technical data sheet values [40,41].

Fig. 20a compares the response of non-toughened and toughened adhesives manufactured through M1 and M2 methods. The fracture behavior of TTM1 and TTM2 were similar, however BBM1 was failed at a lower force than BBM2 adhesive. This behavior can be corelated to the orientation of glass fiber at the middle section. Further, the failure images of the tested specimen are depicted in Fig. 20b. TBM1, TTM1 and TTM2 adhesives were shown a higher whitening area, implicating higher plastic deformation of the adhesives.

The fracture surface of the adhesives experimented under SENB loading was analyzed through SEM images and it reveals different toughening mechanisms. The crack propagation direction in all the images was from the right to the left side, as indicated by the arrow in Fig. 21a. Fig. 21a and b shows the fracture surface of BBM1 adhesive where the glass fiber filler and non-fibrous fillers were identified by the cylindrical and irregular polygon shapes, respectively. These fillers or extenders not only improve the mechanical properties but also increase the viscosity. The glass fibers aligned along the crack path direction exhibited fiber debonding and less K_{IC} as compared with BBM2 adhesive. Fig. 21c and d shows the fracture surface of BTM1 adhesive that was similar to BBM1 adhesive but with more fiber breakages. Fig. 21e depicts a very less amount of the fibers in TBM1 adhesives because of the hybridization and Fig. 21f shows the river-bed morphology and a submicron size (<1 μm) toughening phase. This phase was not visible in μCT images, as the voxel size of the scan was limited to 3.5 μm.

Fig. 22a shows the fracture surface of the toughened adhesive, TTM1 which was very rough and highly textured due to the torturous crack path. A core-shell rubber particle is shown in Fig. 22a where the crack was penetrated through the shell layer and torn into two parts. The

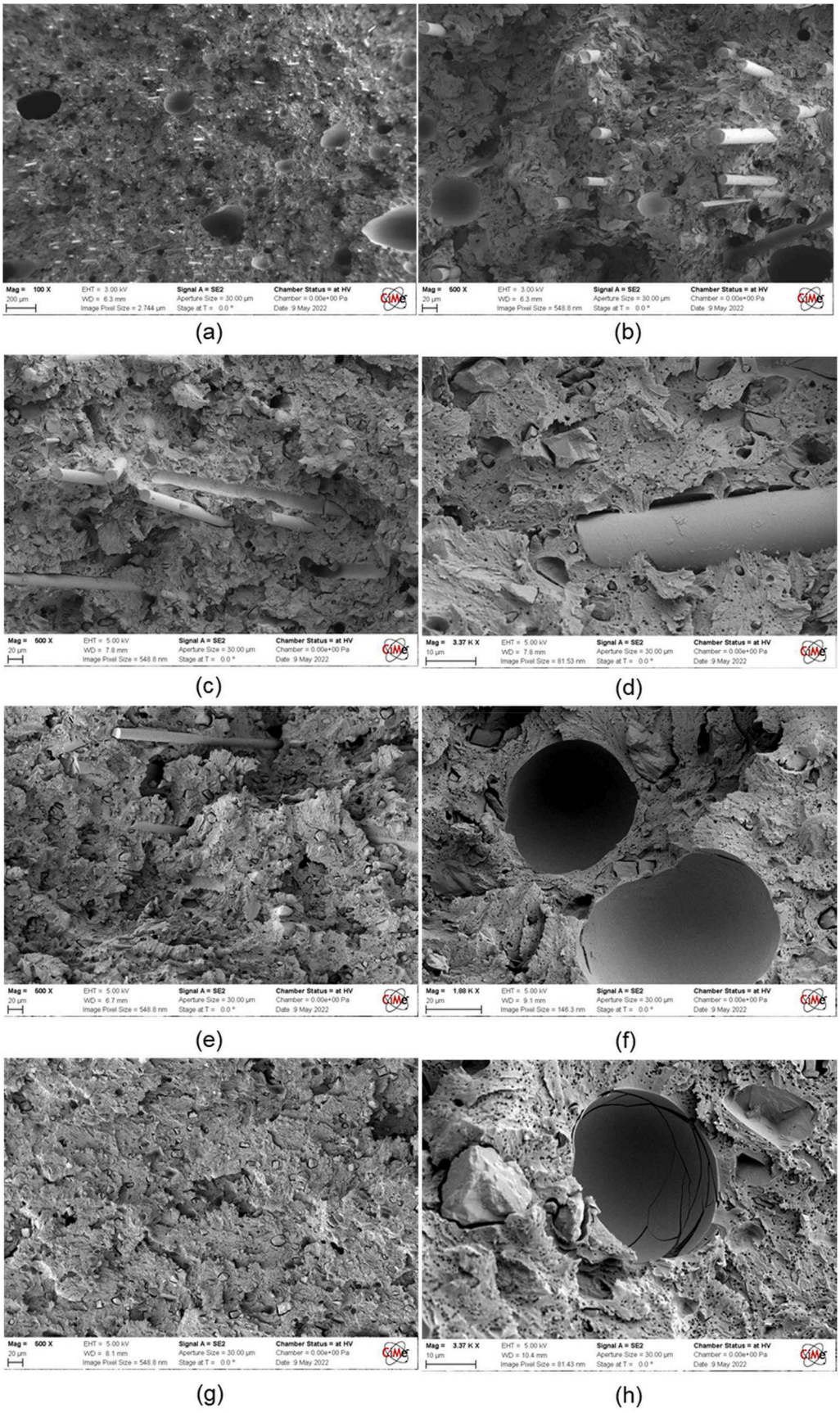

Fig. 23. SEM images of fractured surface of M2 adhesives: (a)&(b) BBM2, (c)&(d) BTM2, (e)&(f) TBM2 and (g)&(h) TTM2.

interface between the shell layer and epoxy adhesive was intact, thanks to the sufficient surface treatment (functionalization) of the particles. As shown in Fig. 22c and d, the core was also severely fractured with multiple tears. The sub-micron size phase and core-shell particle were contributed to the different toughening mechanisms such as multiple crack formation and coalescence, crack tip blunting, crack deflection from the initial fracture plane, and resulting in higher plastic strain and smooth crack propagation. Specifically, a smaller drop in force was noticed before the peak value due to the crack initiation (Fig. 20a). However, further propagation was resisted by the toughened adhesive and gradual decrease in the load was observed, thanks to the multiple toughening mechanisms.

The fracture surface of BBM2 adhesives depicted in Fig. 23a reveals the glass fibers, non-fibrous filler, and the presence of voids due to the manual mixing process. Glass fibers aligned perpendicular to the crack path were contributed to fiber-bridging and higher fracture toughness (43.48% as compared to BBM1 adhesive). It infers that the fracture toughness of the non-toughened adhesive is more sensitive to the glass fiber alignment than the tensile and shear properties. Fig. 23c, d, 23e and 23f illustrate the fracture surface of hybrid adhesives, BTM2 and TBM2. As the toughening increases, the roughness of the fracture surface was also increased. Fig. 23g and f reveal the failure surface of TTM2 adhesive where multiple cracks were noticed in the shell surface of rubber particle.

5. Conclusions

Two different hybridization strategies and manufacturing methods were explored and their effect on the wind turbine blade epoxy adhesive properties was determined through various tests. The following conclusions are being made:

a) There was no significant effect of mechanical dispensing and manual mixing methods on the adhesive strength and modulus values. The latter method can be used to assess the static performance of bulk adhesives. However, the quality of specimens produced by the manual mixing method depends on the individual user and mold geometry.
b) The tensile toughness and strain to failure are improved through toughening, at the expense of decrease in strength and modulus values. The glass transition temperature is not affected either by toughening or manufacturing method. Therefore, these adhesives can be used together in the wind turbine blade based on the load distribution. In this case, the joint performance can be increased at a lower cost.
c) Improper orientation of short glass fiber fillers in the adhesives would result poor fiber bridging and decreases the tensile strength and critical fracture toughness. Interestingly, the shear strength is not influenced by the fiber orientation.
d) The measured properties can be exploited for finite element modelling of the thick adhesive joints behavior.

Declaration of competing interest

The authors declare that they have no known competing financial interests or personal relationships that could have appeared to influence the work reported in this paper.

Data availability

The authors are processing the data and will prepare a data in brief paper soon

Acknowledgement

The authors wish to acknowledge the support and funding of this research by the Swiss National Science Foundation (Grant No. IZCOZ0_189905, https://www.snf.ch/en) under the project, Bonded composite primary structures in engineering applications (BONDS), the assistance provided by the technical team of the structural engineering experimental platform (GIS-ENAC) at the Ecole Polytechnique Fédérale de Lausanne (EPFL), Switzerland and Gurit UK Ltd for providing the adhesive materials and for many helpful discussions. This article/publication is based upon work from COST Action CA18120 (CERTBOND - https://certbond.eu/), supported by COST (European Cooperation in Science and Technology).

References

[1] I. Energy Agency, Review 2021 Assessing the effects of economic recoveries on global energy demand and CO 2 emissions in 2021 Global Energy, Accessed: Jun. 21, 2022. [Online]. Available, www.iea.org/t&c/, 2021.
[2] Global wind report 2021 - global wind energy council, accessed Jun. 24, 2022, https://gwec.net/global-wind-report-2021/.
[3] X. Chen, Experimental investigation on structural collapse of a large composite wind turbine blade under combined bending and torsion, Compos. Struct. 160 (Jan. 2017) 435–445, https://doi.org/10.1016/J.COMPSTRUCT.2016.10.086.
[4] Y.J. Jang, C.W. Choi, J.H. Lee, K.W. Kang, Development of fatigue life prediction method and effect of 10-minute mean wind speed distribution on fatigue life of small wind turbine composite blade, Renew. Energy 79 (1) (Jul. 2015) 187–198, https://doi.org/10.1016/J.RENENE.2014.10.006.
[5] M.A. Eder, R.D. Bitsche, Fracture analysis of adhesive joints in wind turbine blades, Wind Energy 18 (6) (Jun. 2015) 1007–1022, https://doi.org/10.1002/WE.1744.
[6] C. Nagel, A. Sondag, M. Brede, Designing adhesively bonded joints for wind turbines, Adhesives in Marine Engineering (Jan. 2012) 46–71, https://doi.org/10.1533/9780857096159.1.46.
[7] Y.M. Ji, K.S. Han, Fracture mechanics approach for failure of adhesive joints in wind turbine blades, Renew. Energy 65 (May 2014) 23–28, https://doi.org/10.1016/j.renene.2013.07.004.
[8] A.P. Vassilopoulos, The history of fiber-reinforced polymer composite laminate fatigue, Int. J. Fatig. 134 (May 2020), 105512, https://doi.org/10.1016/J.IJFATIGUE.2020.105512.
[9] K.P. Subrahmanian, F. Dubouloz, Adhesives for bonding wind turbine blades, Reinforc Plast 53 (1) (Jan. 2009) 26–29, https://doi.org/10.1016/S0034-3617(09)70044-X.
[10] S.R. Mousavi, et al., Toughening of epoxy resin systems using core–shell rubber particles: a literature review, J. Mater. Sci. 56 (33) (Nov. 2021) 18345–18367, https://doi.org/10.1007/S10853-021-06329-8.
[11] G. Giannakopoulos, K. Masania, A.C. Taylor, Toughening of epoxy using core-shell particles, J. Mater. Sci. 46 (2) (Jan. 2011) 327, https://doi.org/10.1007/s10853-010-4816-6.
[12] A.J. Kinloch, M.L. Yuen, S.D. Jenkins, Thermoplastic-toughened epoxy polymers, J. Mater. Sci. 29 (14) (Jan. 1994) 3781, https://doi.org/10.1007/bf00357349.
[13] B.J. Cardwell, A.F. Yee, Toughening of epoxies through thermoplastic crack bridging, J. Mater. Sci. 33 (22) (1998) 5473, https://doi.org/10.1023/a:1004427123388.
[14] A.Q. Barbosa, L.F.M. da Silva, J. Abenojar, M. Figueiredo, A. Öchsner, Toughness of a brittle epoxy resin reinforced with micro cork particles: effect of size, amount and surface treatment, Compos. B Eng. 114 (Apr. 2017) 299–310, https://doi.org/10.1016/J.COMPOSITESB.2016.10.072.
[15] A.J. Kinloch, J.H. Lee, A.C. Taylor, S. Sprenger, C. Eger, D. Egan, Toughening Structural Adhesives via Nano- and Micro-phase Inclusions, vol. 79, Aug. 2010, pp. 867–873, https://doi.org/10.1080/00218460309551, no. 8–9.
[16] H.M. Chong, A.C. Taylor, The microstructure and fracture performance of styrene-butadiene- methylmethacrylate block copolymer-modified epoxy polymers, J. Mater. Sci. 48 (19) (Oct. 2013) 6762–6777, https://doi.org/10.1007/S10853-013-7481-8/FIGURES/13.
[17] Y. Huang, D.L. Hunston, A.J. Kinloch, C.K. Riew, Mechanisms of toughening thermoset resins, Accessed: Feb. 02, 2022. [Online]. Available: https://pubs.acs.org/sharingguidelines, 1993.
[18] A.J. Kinloch, S.H. Lee, A.C. Taylor, Improving the fracture toughness and the cyclic-fatigue resistance of epoxy-polymer blends, Polymer (Guildf) 55 (24) (Nov. 2014) 6325–6334, https://doi.org/10.1016/J.POLYMER.2014.10.018.
[19] S. Li, Q. Lin, C. Cui, The effect of core–shell particles on the mechanical performance of epoxy resins modified with hyperbranched polymers, J. Mater. Res. 31 (10) (May 2016) 1393–1402, https://doi.org/10.1557/JMR.2016.174.
[20] A.G. Cassano, S. Dev, M. Maiaru, C.J. Hansen, S.E. Stapleton, Cure simulations of thick adhesive bondlines for wind energy applications, J. Appl. Polym. Sci. 138 (10) (Mar. 2021), 49989, https://doi.org/10.1002/APP.49989.
[21] DNV.GL type Approval, Spabond 820HTA, Accessed: Feb. 10, 2022. [Online]. Available, https://www.gurit.com/en/our-business/composite-materials/adhesive-systems, 2021.
[22] DNV.GL type Approval, Spabond 840HTA, Accessed: Feb. 10, 2022. [Online]. Available, https://www.gurit.com/en/our-business/composite-materials/adhesive-systems, 2021.
[23] New certification scheme for type and component certification of wind turbines. https://www.dnv.com/article/new-certification-scheme-for-type-and-component-certification-of-wind-turbines-77500. (Accessed 4 February 2022).

[24] D.V. Srinivasan, V. Ravichandran, S. Idapalapati, Failure analysis of GFRP single lap joints tailored with a combination of tough epoxy and hyperelastic adhesives, Compos. B Eng. 200 (Nov. 2020), 108255, https://doi.org/10.1016/J.COMPOSITESB.2020.108255.
[25] E.A.S. Marques, L.F.M. da Silva, M. Flaviani, Testing and simulation of mixed adhesive joints for aerospace applications, Compos. B Eng. 74 (Jun. 2015) 123–130, https://doi.org/10.1016/J.COMPOSITESB.2015.01.005.
[26] M.D. Fitton, J.G. Broughton, Variable modulus adhesives: an approach to optimised joint performance, Int. J. Adhesion Adhes. 25 (4) (Aug. 2005) 329–336, https://doi.org/10.1016/J.IJADHADH.2004.08.002.
[27] R. Lopes Fernandes, M.K. Budzik, R. Benedictus, S. Teixeira de Freitas, Multi-material adhesive joints with thick bond-lines: crack onset and crack deflection, Compos. Struct. 266 (Jun. 2021), 113687, https://doi.org/10.1016/J.COMPSTRUCT.2021.113687.
[28] J.F. Durodola, Functionally graded adhesive joints – a review and prospects, Int. J. Adhesion Adhes. 76 (Jul. 2017) 83–89, https://doi.org/10.1016/J.IJADHADH.2017.02.008.
[29] N. Burst, D.O. Adams, H.E. Gascoigne, Investigating the Thin-Film versus Bulk Material Properties of Structural Adhesives, vol. 87, Jan. 2011, pp. 72–92, https://doi.org/10.1080/00218464.2011.538326, no. 1.
[30] M. Wentingmann, N. Manousides, A. Antoniou, C. Balzani, Yield surface derivation for a structural adhesive based on multiaxial experiments, Polym. Test. 113 (Sep. 2022), 107648, https://doi.org/10.1016/J.POLYMERTESTING.2022.107648.
[31] P. Zuo, A.P. Vassilopoulos, Review of Fatigue of Bulk Structural Adhesives and Thick Adhesive Joints, vol. 66, 2020, pp. 313–338, https://doi.org/10.1080/09506608.2020.1845110, no. 5.
[32] M. Wentingmann, N. Manousides, A. Antoniou, C. Balzani, Design and manufacturing optimization of epoxy-based adhesive specimens for multiaxial tests, Mater. Des. 212 (Dec. 2021), 110213, https://doi.org/10.1016/J.MATDES.2021.110213.
[33] K.B. Katnam, J.P.J. Stevenson, W.F. Stanley, M. Buggy, T.M. Young, Tensile strength of two-part epoxy paste adhesives: influence of mixing technique and micro-void formation, Int. J. Adhesion Adhes. 31 (7) (Oct. 2011) 666–673, https://doi.org/10.1016/J.IJADHADH.2011.06.005.
[34] G. Fernandez, D. Vandepitte, H. Usabiaga, S. Debruyne, Static and cyclic strength properties of brittle adhesives with porosity, Int. J. Fatig. 117 (Dec. 2018) 340–351, https://doi.org/10.1016/j.ijfatigue.2018.08.018.
[35] A.I.M. Foletti, J. Sena Cruz, A.P. Vassilopoulos, Fabrication and curing conditions effects on the fatigue behavior of a structural adhesive, Int. J. Fatig. 139 (Oct. 2020), 105743, https://doi.org/10.1016/J.IJFATIGUE.2020.105743.
[36] O. Moussa, A.P. Vassilopoulos, J. de Castro, T. Keller, Long-term development of thermophysical and mechanical properties of cold-curing structural adhesives due to post-curing, J. Appl. Polym. Sci. 127 (4) (Feb. 2013) 2490–2496, https://doi.org/10.1002/APP.37965.
[37] E. Sancaktar, H. Jozavi, R.M. Klein, The effects of cure temperature and time on the bulk tensile properties of a structural adhesive, J. Adhes. 15 (3–4) (1983) 241–264, https://doi.org/10.1080/00218468308073230.
[38] M. Savvilotidou, T. Keller, A.P. Vassilopoulos, Fatigue performance of a cold-curing structural epoxy adhesive subjected to moist environments, Int. J. Fatig. 103 (Oct. 2017) 405–414, https://doi.org/10.1016/J.IJFATIGUE.2017.06.022.
[39] M. Savvilotidou, A.P. Vassilopoulos, M. Frigione, T. Keller, Effects of aging in dry environment on physical and mechanical properties of a cold-curing structural epoxy adhesive for bridge construction, Construct. Build. Mater. 140 (Jun. 2017) 552–561, https://doi.org/10.1016/J.CONBUILDMAT.2017.02.063.
[40] SPABOND 820HTA™ Fast curing structural epoxy adhesive, *Full general datasheet*, [Online]. Available, www.gurit.com.
[41] SPABOND™ 840HTA fast curing structural epoxy adhesive, *Full general datasheet*, [Online]. Available, www.gurit.com.
[42] ASTM International, D7028 − 07 Standard Test Method for Glass Transition Temperature (DMA Tg) of Polymer Matrix Composites by Dynamic Mechanical Analysis (DMA), 2007, https://doi.org/10.1520/D7028-07E01R15.
[43] ASTM International, Standard Test Method for Tensile Properties of Plastics, 2014, https://doi.org/10.1520/D0638-14.
[44] ASTM International, Standard Test Method for Shear Properties of Composite Materials by the V-Notched Beam Method, 2019, https://doi.org/10.1520/D5379_D5379M-19E01.
[45] ASTM International, Standard Test Methods for Plane-Strain Fracture Toughness and Strain Energy Release Rate of Plastic Materials, 2014, https://doi.org/10.1520/D5045-14.
[46] J. Schalnat, D.G. Gómez, L. Daelemans, I. de Baere, K. de Clerck, W. van Paepegem, Influencing parameters on measurement accuracy in dynamic mechanical analysis of thermoplastic polymers and their composites, Polym. Test. 91 (Nov. 2020), 106799, https://doi.org/10.1016/J.POLYMERTESTING.2020.106799.
[47] K.P. Menard, Dynamic Mechanical Analysis : A Practical Introduction, second ed., May 2008, https://doi.org/10.1201/9781420053135.
[48] V. Perruchoud, A.P. Vassilopoulos, The challenges of quasi-static and fatigue experiments of structural adhesives, Int. J. Fatig. 162 (Sep. 2022), 106980, https://doi.org/10.1016/J.IJFATIGUE.2022.106980.
[49] K. Ravi-Chandar, W.G. Knauss, An experimental investigation into dynamic fracture: III. On steady-state crack propagation and crack branching, Int. J. Fract. 26 (2) (Oct. 1984) 141–154, https://doi.org/10.1007/BF01157550, 1984 26:2.
[50] C.Y. Chiem, Z.G. Liu, The relationship between tensile strength and shear strength in composite materials subjected to high strain rates, J. Eng. Mater. Technol. 110 (2) (Apr. 1988) 191–194, https://doi.org/10.1115/1.3226030.